

Cooperative Jahn-Teller distortion in PrO₂C. H. Gardiner,^{1,*} A. T. Boothroyd,² P. Pattison,³ M. J. McKelvy,⁴ G. J. McIntyre,⁵ and S. J. S. Lister⁶¹*National Physical Laboratory, Queens Road, Teddington, Middlesex TW11 0LW, United Kingdom*²*Clarendon Laboratory, University of Oxford, Parks Road, Oxford OX1 3PU, United Kingdom*³*Swiss-Norwegian Beamline, European Synchrotron Radiation Facility, Boîte Postale 220, F-38043 Grenoble Cédex 9, France*⁴*Center for Solid State Science, Arizona State University, Tempe, Arizona 85287-1704, USA*⁵*Institut Laue-Langevin, Boîte Postale 156, F-38042 Grenoble Cédex 9, France*⁶*Oxford Magnet Technology Ltd., Wharf Road, Eynsham, Witney, Oxfordshire OX29 4BP, United Kingdom*

(Received 9 November 2003; revised manuscript received 23 February 2004; published 27 July 2004)

We report neutron diffraction data on single crystal PrO₂ which reveal a cooperative Jahn-Teller distortion at $T_D = 120 \pm 2$ K. Below this temperature an internal distortion of the oxygen sublattice causes the unit cell of the crystallographic structure to become doubled along one crystal axis. We discuss several possible models for this structure. The antiferromagnetic structure below $T_N = 13.5$ K is found to consist of two components, one of which shares the same doubled unit cell as the distorted crystallographic structure. We also present measurements of the magnetic susceptibility, the specific heat capacity, and the electrical conductivity of PrO₂. The susceptibility data show an anomaly at a temperature close to T_D . From the specific heat capacity data we deduce that the ground state is doubly degenerate, consistent with a distortion of the cubic local symmetry. We discuss possible mechanisms for this. The conductivity shows an activated behavior with an activation energy $E_a = 0.262 \pm 0.003$ eV.

DOI: 10.1103/PhysRevB.70.024415

PACS number(s): 61.66.Fn, 75.25.+z, 75.30.Cr, 75.40.Cx

I. INTRODUCTION

In recent years there has been a resurgence of interest in phenomena associated with orbital degrees of freedom,¹ such as orbital ordering, orbital waves (“orbitons”),² and unusual spin-orbital liquid ground states.^{3,4} Much of the work has been stimulated by studies of the perovskite-based transition-metal oxides, e.g., the colossal magnetoresistance manganites, whose properties can be strongly influenced by the extent to which orbital degrees of freedom are quenched by Jahn-Teller distortions of the lattice or coupled to other electronic degrees of freedom.

Jahn-Teller and orbital phenomena also occur in compounds containing localized $4f$ and $5f$ electrons. Among the simplest of these, the fluorite-structure actinide dioxides UO₂ and NpO₂ have been investigated for many years,^{5,6} and are now understood to exhibit complex ordered phases at low temperatures involving coupled electric and magnetic multipoles as well as (in the case of UO₂) a lattice distortion.

Unusual magnetic effects have also been found in the fluorite-structure lanthanide dioxide PrO₂. Some years ago, PrO₂ was found to have an anomalously small ordered moment in the antiferromagnetic phase.⁷ Very recently, we discovered a broad continuum in the magnetic excitation spectrum of PrO₂ probed by neutron inelastic scattering, which we ascribed to Jahn-Teller fluctuations involving the orbitally degenerate $4f$ ground state and dynamic distortions of the lattice.⁸ In a separate neutron diffraction experiment⁹ we found evidence that the antiferromagnetic structure contains a component with twice the periodicity of the accepted type-I magnetic structure.⁷

In this paper we follow up our previous work^{8,9} with further experimental results on the electronic and magnetic behaviour of PrO₂. Our main results come from neutron and x-ray diffraction measurements of the crystallographic and

magnetic structure of PrO₂ in the temperature range 2–300 K. These reveal the existence of an internal distortion of the fluorite structure below $T_D = 120$ K and a related distortion of the antiferromagnetic structure below $T_N = 13.5$ K. We also report measurements of the magnetic susceptibility, the specific heat capacity, and the electrical conductivity of PrO₂, which allow us to determine the effective paramagnetic moment of the Pr ion, the degeneracy of the $4f$ electron ground state, and the activation energy of the charge carriers.

II. SAMPLE PREPARATION

Measurements were made on single crystal and polycrystalline samples of PrO₂. The single crystals used for the neutron diffraction and conductivity measurements were taken from a batch prepared several years ago by a hydrothermal procedure.¹⁰ The sample used for neutron diffraction was the largest of the batch, with a mass of ≈ 1 mg, while the sample used for the conductivity measurements was somewhat smaller. Both were irregularly shaped. Polycrystalline samples were used for the x-ray diffraction, magnetic susceptibility, and specific heat capacity measurements. These were prepared by oxidation of commercially obtained Pr₆O₁₁. The starting powder was first baked in air at 1000 °C for ~ 11 h and then annealed in flowing oxygen at 280 °C for 30 days. The powder was reground approximately once a week during the annealing. Synchrotron x-ray diffraction showed that the final product contained $\sim 1\%$ of residual Pr₆O₁₁.

III. STRUCTURAL INVESTIGATION

We investigated the crystallographic and magnetic structure of PrO₂ by performing a neutron diffraction study on a

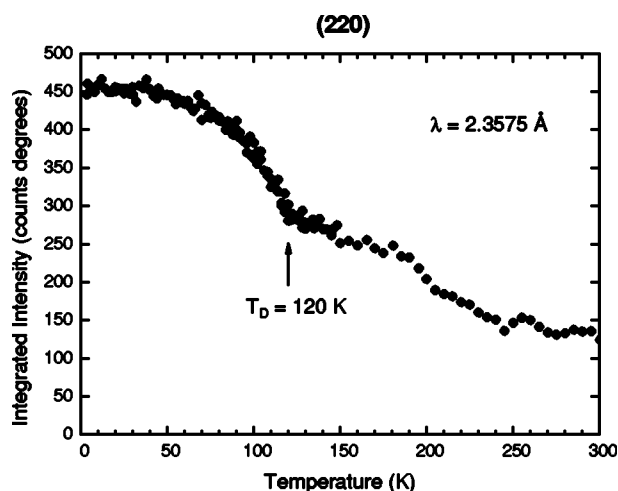


FIG. 1. Temperature dependence of the (220) reflection.

single crystal sample. The experiment was carried out on the D10 four-circle diffractometer at the Institut Laue-Langevin. We used an Eulerian cradle for crystal orientation and a position sensitive detector. The latter was kept in the scattering plane at all times. The diffractometer configuration was as follows: a vertically curved pyrolytic graphite (002) or Cu (200) monochromator, no collimators, a circular aperture of diameter 6 mm before the sample, and a rectangular aperture of dimensions 20 mm \times 25 mm before the detector. We used incident neutron wavelengths of 2.3575 Å (λ_1) and 1.2579 Å (λ_2) from the pyrolytic graphite and Cu monochromators, respectively, with a pyrolytic graphite filter for the former to reduce the half-wavelength contribution. The larger wavelength provided greater flux, while the smaller provided greater coverage of reciprocal space.

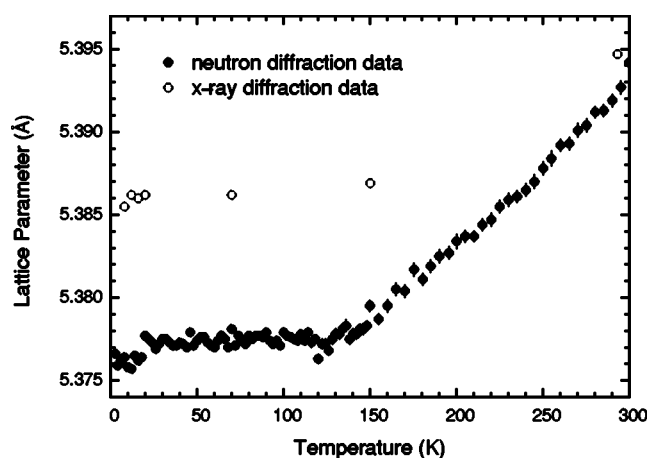
The single crystal sample was mounted on a thin aluminum pin and aligned such that the $[1\bar{1}0]$ direction lay along the axis of the pin. The pin was attached to the Eulerian cradle inside a helium flow cryostat.

A. Measurements

The quality of the crystal was checked by performing crystal rotation scans (ω scans) of the strongest structural Bragg reflections at room temperature. The peak widths were found to be within the experimental resolution.

To examine the crystallographic structure of PrO₂, as many structural Bragg reflections as possible were measured by ω scan at the accessible positions in reciprocal space satisfying the selection rules for the fluorite structure (h , k , and l all even or all odd). This set of reflections was measured at λ_1 at temperatures of 2 K, 20 K, 90 K, 150 K, and 300 K. At some temperatures the full set was measured at both neutron wavelengths (λ_1 and λ_2).

The intensities of the strongest reflections [e.g., (220), (400)] were found to change rapidly with temperature. The temperature dependence of these reflections was measured more carefully by performing ω scans at 2 K intervals between 2 K and 130 K and then at 5 K intervals between 130 K and 300 K. Figure 1 shows the integrated intensity of the

FIG. 2. Temperature dependence of the lattice parameter in PrO₂.

the scan as a function of temperature. A sharp rise in intensity can be seen below 120 K. We found that the rise was greatest for the strongest reflections and more pronounced at the larger wavelength λ_1 , suggesting a sudden reduction in extinction. A possible explanation for this observation is a reduction in grain size caused by the strain associated with a structural distortion.

The temperature dependence of the lattice parameter, estimated from the variation of the Bragg angle with temperature for the (400) reflection, also shows a sharp change at \sim 120 K (see Fig. 2, closed circles). Although the absolute value of the lattice parameter obtained by this method is inaccurate, as it relies on the crystal being perfectly aligned, the data nevertheless give a good qualitative indication of the way the lattice parameter changes with temperature. It is seen to decrease linearly from 300 K to \sim 120 K, below which it becomes approximately constant, dipping slightly at \sim 18 K. The open circles in Fig. 2 show data taken from a high-resolution x-ray powder diffraction study on PrO₂ performed at the Swiss-Norwegian Beamline BM1B at the European Synchrotron Radiation Facility (ESRF). There are fewer points in this plot, but the absolute value of the lattice parameter is much more accurate because it has been obtained by Rietveld refinement of the diffraction pattern. The temperature variation found by x-ray diffraction is consistent with that found by neutron diffraction.

To probe the magnetic structure, as many magnetic Bragg reflections as possible were measured by ω scan at the accessible positions in reciprocal space satisfying the selection rules for the antiferromagnetic (AFM) type-I magnetic structure (h , k , and l a mixture of even and odd). This set of reflections was measured at temperatures of 2 K and 20 K (below and above T_N) using only the larger wavelength λ_1 , since this provided higher flux.

In addition to the above measurements we also performed ω scans at a number of positions in reciprocal space with half-integer Miller indices. The object of these measurements was to search for peaks seen previously in a powder diffraction experiment.⁹ The scans were performed at temperatures of 2 K, 20 K, and 150 K.

At $T=2$ K, we found reflections at positions satisfying the selection rule $h=n+1/2$, $k=\text{odd}$, $l=\text{even}$, where n , k , and l

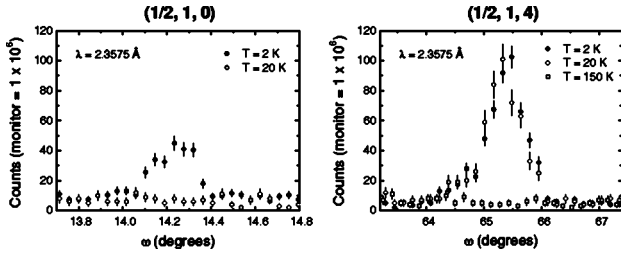


FIG. 3. ω scans of typical half-integer reflections (detector counts are normalized to a fixed incident beam monitor count of 1×10^6 , corresponding to a counting time of ~ 100 s). Those reflections with $l=0$ are absent above T_N . Those with $l \neq 0$ are still present above T_N . All are absent at $T=150$ K.

are integers, and h , k , and l can be commuted. At $T=20$ K (above T_N), we found reflections at exactly the same positions, except that those with $l=0$ were no longer present. The strongest half-integer reflection we observed was $\sim 1\%$ of the intensity of the strongest fluorite reflection. At $T=150$ K, all the half-integer reflections had disappeared. Figure 3 shows ω scans of the $(\frac{1}{2}10)$ and $(\frac{1}{2}14)$ reflections. These are typical of the two observed sets of half-integer reflections: those with $l=0$ and those with $l \neq 0$.

We measured the temperature dependence of the $(\frac{1}{2}10)$ reflection by counting at the peak center at a series of temperatures between 2 K and 20 K. The temperature dependence of the stronger $(\frac{1}{2}14)$ reflection was measured by performing ω scans at a series of temperatures between 2 K and 150 K.

Figure 4 compares the temperature dependence of the $(\frac{1}{2}10)$ reflection with that of the magnetic reflection (100). To within experimental uncertainty, both reflections disappear at the antiferromagnetic ordering temperature T_N . We were able to determine T_N for both reflections by fitting the data using order parameter curves of the form

$$I \propto (T_N - T)^{2\beta}, \quad (1)$$

where I is the peak count and β is the critical exponent. For the (100) reflection we found $T_N = 13.41 \pm 0.04$ K, while for the $(\frac{1}{2}10)$ reflection we found $T_N = 13.5 \pm 0.2$ K. Since these are in excellent agreement, it is likely that both reflections are magnetic in origin and belong to the same magnetic phase. The existence of half-integer magnetic Bragg reflections indicates that the magnetic unit cell is doubled along one crystal axis.

Figure 5 shows the temperature dependence of the $(\frac{1}{2}14)$ reflection. It is found to disappear at $T_D = 120 \pm 2$ K, which is the same as the temperature below which we observed a sharp rise in the intensities of the large structural reflections. This strongly suggests that the $(\frac{1}{2}14)$ reflection is structural in origin. The existence of half-integer structural reflections indicates that the crystallographic unit cell is also doubled along one crystal axis.

A reexamination of previous data taken with a powder sample on the POLARIS diffractometer at the ISIS facility⁹ has now also revealed half-integer structural reflections. Although two of the magnetic half-integer reflections had been

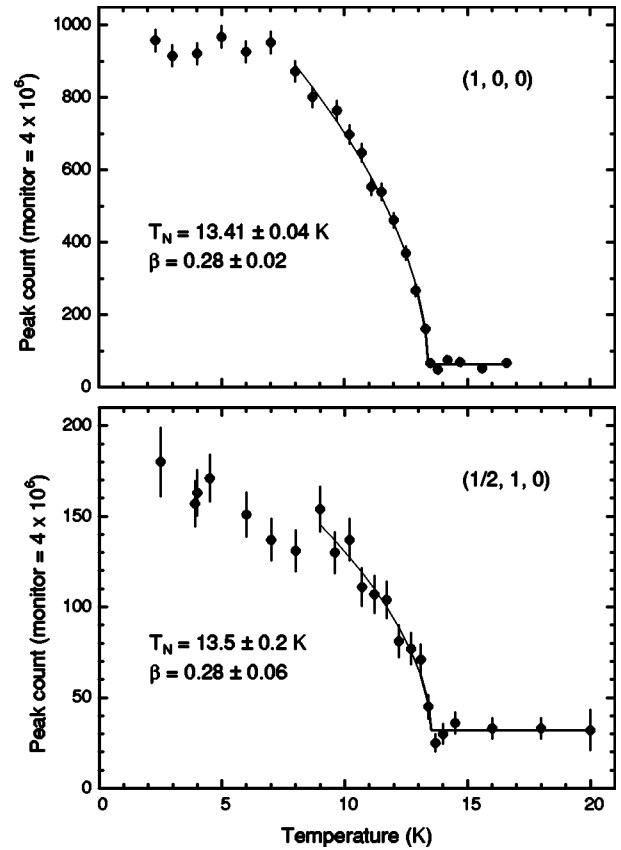


FIG. 4. Temperature dependence of the $(\frac{1}{2}10)$ and (100) intensities (detector counts are normalized to a fixed incident beam monitor count of 4×10^6 , corresponding to a counting time of ~ 8 min in the upper graph and ~ 6.5 min in the lower graph). Order parameter curves of the form $I \propto (T_N - T)^{2\beta}$ have been fitted to the data to determine T_N . Note that the temperature dependence of the (100) reflection was actually measured during an earlier experiment performed on the same instrument with the same crystal, but with a different sample environment, so the intensities in the two plots should not be compared directly.

seen previously, the structural reflections had not been noticed, due to the nearby presence of other peaks of similar intensity, which were probably due to scattering from the sample environment. The x-ray powder diffraction study mentioned above also confirms the presence of half-integer structural reflections.

B. Structure analysis

To identify the nature of the crystallographic structure below $T_D = 120$ K and the magnetic structure below $T_N = 13.5$ K, we performed a detailed analysis of the intensities of the observed integer and half-integer structural and magnetic reflections at low temperatures.

After background subtraction, each ω scan was integrated using the extended trapezoidal rule¹¹ (a simple method of numerical integration), corrected for the Lorentz factor, normalized to the monitor count and the intensity of the (311) reflection, and multiplied by a wavelength-dependent scale factor to enable direct comparison between the intensities of

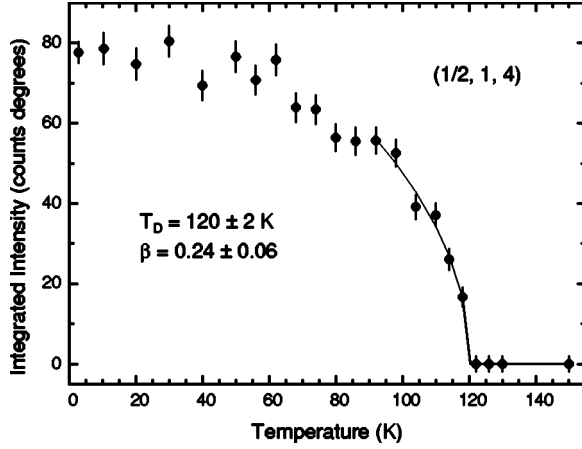


FIG. 5. Temperature dependence of the $(\frac{1}{2}, 1, 4)$ intensity. An order parameter curve of the form $I \propto (T_D - T)^{2\beta}$ has been fitted to the data to determine T_D .

the observed structural reflections and their calculated structure factors. The (311) reflection was used for normalization because it was one of the weakest reflections accessible at both wavelengths, so it was little affected by extinction. In addition, its structure factor contained no contribution from the oxygen ions, so it was unaffected by the distortion. Finally, the corrected and scaled intensities were averaged over symmetry-equivalent reflections to guard against the possibility that a chance uneven distribution in symmetry-equivalent structural or magnetic domain populations might affect the measured intensity of any given reflection (although this was unlikely since the majority of the symmetry-equivalent reflections were equal in intensity to within experimental uncertainty).

We then considered distortions of the fluorite crystallographic structure and the type-I antiferromagnetic structure which would give rise to structure factors in agreement with the relative intensities and selection rules of the observed reflections. Such structures were identified by trial and error. However, in the case of the crystallographic structure we were guided by the results of the x-ray diffraction study, which revealed no splitting of the reflections caused by the fluorite structure. This indicated that the Pr lattice remained undisturbed, and any distortion must therefore be due to an internal rearrangement of the oxygen atoms.

Once a suitable distorted crystallographic structure was found, we refined the overall magnitude of the oxygen displacements by a least squares method to achieve the best possible agreement between the structure factors and peak intensities. For the magnetic structure we used the ratio of the peak intensity to the magnetic structure factor for each reflection to obtain a value for the ordered moment μ of the Pr ion.

The structure factors of the structural reflections are given by

$$|F_N(\mathbf{Q})|^2 = \left| \sum_j \langle \bar{b}_j e^{i\mathbf{Q} \cdot \mathbf{r}_j} e^{-W_j(Q,T)} \rangle \right|^2, \quad (2)$$

where the summation index j runs over all the atoms in the unit cell, \bar{b}_j is the nuclear scattering length of the j th atom

averaged over all of its isotopes, \mathbf{r}_j is the position of the j th atom within the unit cell, $e^{-W_j(Q,T)}$ is the Debye-Waller factor (we set this equal to 1, since the measurements were made at low temperatures), and $\langle \rangle$ denotes an average over all symmetry-equivalent structural domains. The scaled, integrated intensities of the structural reflections are equal to $|F_N(\mathbf{Q})|^2$. The structure factors of the magnetic reflections are given by

$$|F_M(\mathbf{Q})|^2 = \sum_{\alpha\beta} \langle (\delta_{\alpha\beta} - \hat{Q}_\alpha \hat{Q}_\beta) F_M^\alpha(\mathbf{Q}) F_M^{\beta*}(\mathbf{Q}) \rangle, \quad (3)$$

where the summation indices α and β run over the Cartesian coordinates x , y , and z , $\delta_{\alpha\beta}$ is the Kronecker delta, the asterisk denotes the complex conjugate, \hat{Q}_α is the α component of the unit scattering vector, and $\langle \rangle$ denotes an average over all symmetry-equivalent magnetic domains. In the dipole approximation $F_M^\alpha(\mathbf{Q})$ is given by

$$F_M^\alpha(\mathbf{Q}) = f(\mathbf{Q}) \sum_j \hat{\mu}_j^\alpha e^{i\mathbf{Q} \cdot \mathbf{r}_j} e^{-W_j(Q,T)}, \quad (4)$$

where the summation index j runs over all the magnetic atoms in the magnetic unit cell, $\hat{\mu}_j^\alpha$ is the α component of a unit vector in the direction of the magnetic moment of the j th magnetic atom, \mathbf{r}_j is the position of the j th magnetic atom within the magnetic unit cell, $f(\mathbf{Q})$ is the magnetic form factor of the Pr^{4+} ion, and $e^{-W_j(Q,T)}$ is the Debye-Waller factor (set equal to 1). The scaled, integrated intensities of the magnetic reflections are proportional to $(\gamma r_0/2)^2 (\mu/\mu_B)^2 |F_M(\mathbf{Q})|^2$, where $(\gamma r_0/2)^2 = 72.4 \text{ m}^2$ ($=7.24 \text{ fm}^2$) and μ_B is the Bohr magneton.

For reference, we note the structure factors of the fluorite structure here:

$$|F_N(\mathbf{Q})|^2 = \begin{cases} 336 \text{ fm}^2, & h, k, l \text{ all odd,} \\ 791 \text{ fm}^2, & h + k + l = 2n, \\ 4194 \text{ fm}^2, & h + k + l = 4n. \end{cases} \quad (5)$$

These were computed using the fluorite unit cell, which contains four Pr ions and eight O ions. For the half-integer reflections (both structural and magnetic) we used a unit cell that was doubled along one axis, thus containing eight Pr ions and sixteen O ions. In order to allow direct comparison with the structure factors of the fluorite structure we divided the structure factors $F_N(\mathbf{Q})$ and $F_M(\mathbf{Q})$ of the half-integer reflections, calculated in the doubled cell, by 2.

1. Distorted crystallographic structure

One of the simplest structures that possesses structure factors in agreement with the intensities of the half-integer structural reflections is shown in Fig. 6(a). The Pr lattice is undisturbed, but the oxygen ions are each displaced by an amount d in a direction perpendicular to that along which the unit cell is doubled (in Fig. 6 the doubling is along the x direction and the displacements are along the y direction). The oxygen cubes in the two halves of the doubled unit cell are sheared in opposite senses, so we will refer to this structure as the “sheared” structure. The space group is $Imcb$ (a variant of $Ibam$, space group 72), with the origin shifted by $\frac{1}{4}$

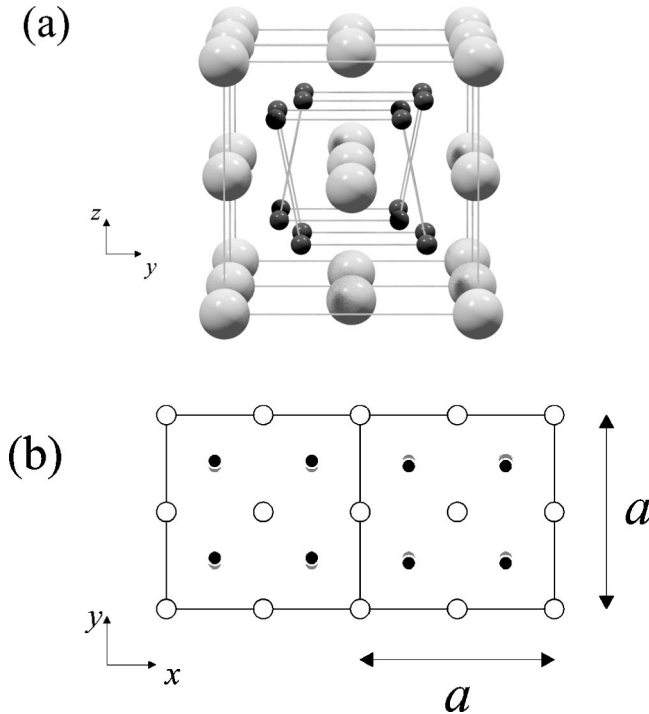


FIG. 6. Sheared structure. (a) The large pale spheres are praseodymium ions and the small dark spheres are oxygen ions. The oxygen cubes in the two halves of the doubled unit cell are sheared in opposite senses, but both have a shearing vector that is perpendicular to the direction along which the cell is doubled. The displacements of the oxygen ions have been exaggerated for clarity. (b) Scale diagram showing the distorted structure in plan view. The white circles are praseodymium ions and the black circles are oxygen ions.

of the unit cell length along the orthorhombic a direction (the x direction in Fig. 6).

A simple least squares refinement of the oxygen displacement d , based on comparison of the domain-averaged structure factors²⁶ and the observed intensities of the half-integer reflections, yielded $d=0.0726(54)$ Å. The structure factors and observed intensities at $T=20$ K are listed in Table I, and a plan view of the structure with displacements to scale is shown in Fig. 6(b). A full crystal structure refinement using the Cambridge Crystallography Subroutine Library (CCSL) yielded $d=0.0664(17)$ Å.

An identical shearing of the oxygen cube was originally proposed for an internal distortion observed in UO₂,¹² although in that compound there was no evidence for a doubling of the unit cell. In UO₂ the oxygen ions are displaced by 0.014 Å from their fluorite structure sites, so the oxygen displacements in PrO₂ are five times as large, and this is reflected in the high value of the transition temperature. It is now accepted that the oxygen configuration in UO₂ forms a triple- \mathbf{q} structure.¹³ However, there is currently no reason to assume that the same is true in PrO₂.

It is interesting to note that there are two distinct Pr sites in the sheared structure, each of which occurs with equal frequency. The two sites have different surrounding oxygen configurations, which are shown in Fig. 7. At one site the oxygens form a parallelohedron (a polyhedron with two

TABLE I. Comparison between $|\frac{1}{2}F_N(\mathbf{Q})|^2$ for the sheared structure and the intensities of the observed half-integer structural reflections at $T=20$ K. The $F_N(\mathbf{Q})$ have been divided by 2, as described in Sec. III B, to allow direct comparison between the two columns.

Reflection	$ \frac{1}{2}F_N(\mathbf{Q}) ^2$ (fm ²)	Intensity (fm ²)
$(\frac{1}{2}10)$	0.0	0.1 ± 0.1
$(\frac{3}{2}10)$	0.0	0.3 ± 0.1
$(\frac{5}{2}10)$	0.0	0.5 ± 0.2
$(\frac{1}{2}12)$	5.1	5.5 ± 0.3
$(\frac{3}{2}12)$	5.1	5.0 ± 0.3
$(\frac{5}{2}12)$	5.1	4.8 ± 0.5
$(\frac{7}{2}12)$	5.1	4.8 ± 0.6
$(\frac{1}{2}14)$	19.9	16.6 ± 0.9
$(\frac{3}{2}14)$	19.9	20.5 ± 1.2
$(\frac{1}{2}16)$	42.7	42.3 ± 2.3
$(\frac{1}{2}30)$	0.0	0.4 ± 0.2
$(\frac{1}{2}32)$	5.1	5.2 ± 0.6
$(\frac{3}{2}32)$	5.1	7.1 ± 0.6
$(\frac{5}{2}32)$	5.1	7.1 ± 1.0
$(\frac{7}{2}32)$	5.1	6.3 ± 1.1
$(\frac{1}{2}34)$	19.9	17.7 ± 1.5
$(\frac{3}{2}34)$	19.9	22.0 ± 1.5
$(\frac{3}{2}36)$	42.7	45.6 ± 3.0
$(\frac{1}{2}52)$	5.1	6.9 ± 1.2
$(\frac{3}{2}52)$	5.1	8.7 ± 1.6
$(\frac{7}{2}52)$	5.1	4.9 ± 1.8
$(\frac{1}{2}72)$	5.1	12.4 ± 2.2

square faces, two rectangular faces, and two parallelogram faces), while at the other they form a polyhedron with four parallelogram faces and four triangular faces.

Although the distorted structure described above is consistent with the intensities of the observed reflections, it is not the only such structure. For example, a superposition of two structures identical to the sheared structure, but with oxygen displacements of 0.0511 Å in mutually perpendicular directions, gives similar agreement between the calculated structure factors and observed intensities. The overall displacement of each oxygen ion in that case is $\sqrt{2} \times 0.0511 = 0.0722$ Å.

The “chiral” structure shown in Fig. 8 is also consistent with the intensities of the observed reflections, and has the

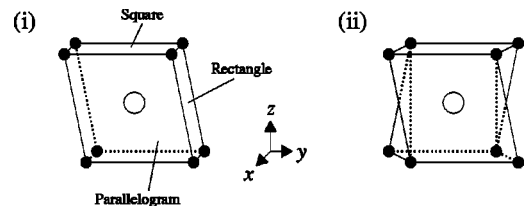


FIG. 7. The two different Pr sites that occur in the sheared structure shown in Fig. 6. The white circles are praseodymium ions and the black circles are oxygen ions. (i) Parallelohedron. (ii) Polyhedron with four parallelogram faces and four triangular faces.

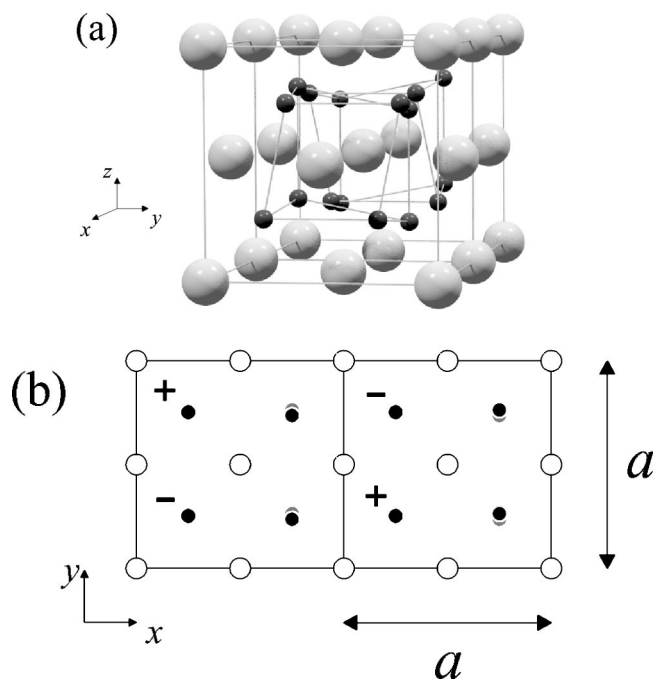


FIG. 8. Chiral distorted structure. (a) The large pale spheres are praseodymium ions and the small dark spheres are oxygen ions. The displacements of the oxygen ions have been exaggerated for clarity. (b) Scale diagram showing the chiral structure in plan view. The white circles are praseodymium ions and the black circles are oxygen ions. The + and - symbols indicate positive and negative displacements along the z direction.

additional advantages of having a lower Jahn-Teller energy¹⁴ and a single Pr site. A chiral model is adopted for the oxygen displacement vector, but the structure factors and the magnitude of the oxygen displacement are almost identical to that of the sheared structure [a simple least squares refinement yielded $d=0.0726(54)$ Å, whereas a full crystal structure refinement using CCSL yielded $d=0.0663(16)$ Å]. The space group is $I4(1)/acd$ (space group 142), with Pr at positions $8a(0, \frac{1}{4}, \frac{3}{8})$ and O at positions $16e(\frac{1}{4}+d, 0, \frac{1}{4})$, where the origin is chosen to be at the center of inversion, and c is the unique axis.

2. Doubled magnetic structure

The presence of half-integer magnetic reflections alongside stronger integer magnetic reflections indicates that the magnetic structure consists of two components: a primary component with the same unit cell as the fluorite structure and a secondary component with a unit cell that is doubled along one crystal axis. This picture fits well with the model of the distorted crystallographic structure, in which the Pr lattice remains unchanged, but the oxygen sublattice undergoes an internal distortion which gives rise to a component of the structure with a doubled unit cell.

The easiest way to analyze the magnetic structure is to consider the two components separately, so that the overall structure can be visualized by performing a vector addition of the two components of the magnetic moment for each Pr ion in the doubled unit cell.

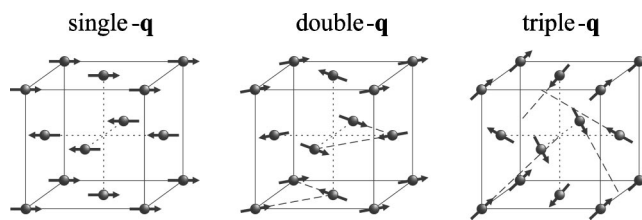


FIG. 9. Type-I primary component of the magnetic structure. Neutron diffraction measurements under ambient conditions cannot distinguish between the multi- \mathbf{q} structures shown, because each gives rise to identical magnetic structure factors when averaged over symmetry-equivalent magnetic domains. However, since the crystallographic unit cell is doubled along one crystal axis, the single- \mathbf{q} structure seems the most likely candidate.

The primary component of the magnetic structure is the AFM type-I structure, shown in Fig. 9. This gives rise to the integer magnetic reflections. Under ambient conditions it is not possible to distinguish between the three multi- \mathbf{q} structures shown in the figure, but in view of the fact that the structural distortion doubles the unit cell along one crystal axis only, the single- \mathbf{q} structure seems the most likely candidate.

The configuration of the magnetic moments in the secondary component of the magnetic structure was deduced using a technique similar to that for the structural distortion. In our search for possible configurations we found it impossible to conceive of a magnetic structure that would give rise to reflections at $l=0$ alone. Symmetry requires that if a structure gives rise to reflections at $l=0$ it will also give rise to reflections at all positions with $l=\text{even}$. This means that many of the magnetic half-integer reflections coincide with the structural ones. However, since little change was observed in the intensities of the structural half-integer reflections below T_N (see Fig. 3), it can be assumed that the magnetic intensities at these positions are much smaller than the structural intensities. We have therefore made no attempt to analyze the magnetic contribution at these positions. Our analysis of the secondary component of the magnetic structure is based solely on the half-integer reflections observed at $l=0$.

The number of possible magnetic structures consistent with the observed half-integer intensities is quite large. Two of the simplest possible structures are shown in Fig. 10. Both possess identical magnetic structure factors, shown in Table II. Figure 10(a) corresponds to the chiral model for the structural distortion shown in Fig. 8, whereas Fig. 10(b) corresponds to the model shown in Fig. 6. The moments of the Pr ions in both magnetic structures point along directions perpendicular to the direction along which the unit cell is doubled. Similar structures in which some or all of the moments point along the doubling direction give poorer agreement with the relative intensities of the observed reflections. It should be mentioned that the $(\frac{5}{2}10)$ reflection had a high and rather sloping background, due to its proximity in reciprocal space to an aluminum powder line, so its intensity is somewhat unreliable.

The magnetic moment of the Pr ion can be calculated for each of the two components of the magnetic structure as follows:

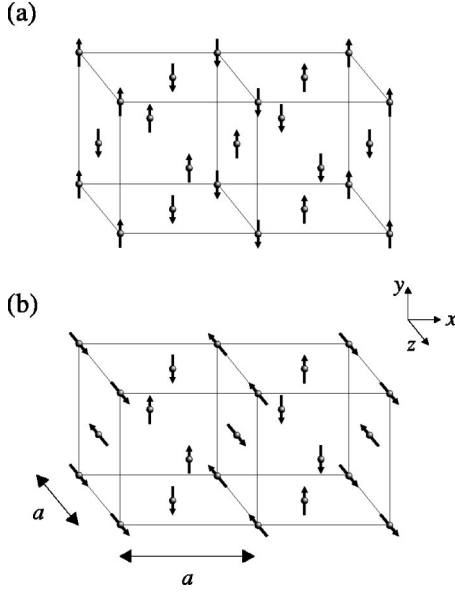


FIG. 10. Possibilities for the secondary component of the magnetic structure. (a) All moments point along the y axis. This structure is associated with the chiral model for the structural distortion shown in Fig. 8. (b) Half the moments point along the y axis and half along the z axis. This structure is associated with the model shown in Fig. 6. The magnetic structure factors of both structures are identical after domain averaging.

$$\frac{\mu}{\mu_B} = \sqrt{\frac{I_M(\mathbf{Q})|F_N(\mathbf{Q}')|^2}{(\gamma r_0/2)^2 I_N(\mathbf{Q}')|F_M(\mathbf{Q})|^2}}, \quad (6)$$

where μ is the magnetic moment of the Pr ion in one component of the magnetic structure, $I_M(\mathbf{Q})$ is the integrated intensity of a magnetic reflection with reciprocal lattice vector \mathbf{Q} , $|F_M(\mathbf{Q})|^2$ is the magnetic structure factor of this reflection, $I_N(\mathbf{Q}')$ is the integrated intensity of a nuclear reflection with reciprocal lattice vector \mathbf{Q}' , and $|F_N(\mathbf{Q}')|^2$ is the nuclear structure factor of this reflection.

For each of the magnetic reflections we calculated the magnetic moment of the Pr ion from the observed magnetic

TABLE II. For the doubled component of the magnetic structure the magnetic structure factors $|\frac{1}{2}F_M(\mathbf{Q})|^2$ (dimensionless) are compared with the magnetic intensities measured at $T=2$ K. The $F_M(\mathbf{Q})$ have been divided by 2, as described in Sec. III B to maintain consistency and with the structural calculations. The ratio of magnetic intensity to magnetic structure factor is constant, and can be used to determine the magnetic moment of the Pr ion as described below.

Reflection	$ \frac{1}{2}F_M(\mathbf{Q}) ^2$	Intensity (fm ²)
$(\frac{1}{2}10)$	1.5	1.4 ± 0.1
$(\frac{3}{2}10)$	1.9	1.7 ± 0.1
$(\frac{5}{2}10)$	1.8	0.9 ± 0.3
$(\frac{1}{2}30)$	0.9	1.1 ± 0.2
$(\frac{3}{2}30)$	1.0	1.1 ± 0.2

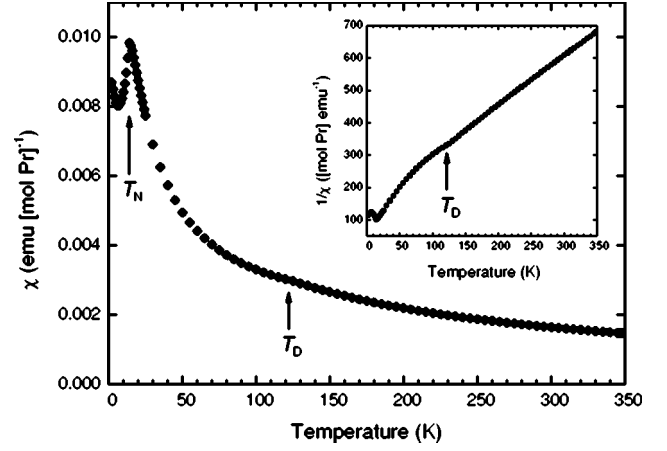


FIG. 11. Magnetic susceptibility of PrO₂ powder. Molar susceptibility is plotted in the main graph and inverse molar susceptibility is shown in the inset.

intensity and the intensity of the (311) nuclear reflection. The resulting values of the Pr moment were averaged to reduce the uncertainty. For the primary (AFM type-I) component of the magnetic structure we obtained $\mu_1 = (0.65 \pm 0.02)\mu_B$. This is in good agreement with a previous value of $(0.68 \pm 0.07)\mu_B$ (Ref. 9) obtained by neutron diffraction from the same single crystal sample. Previous powder diffraction experiments have yielded values of $(0.6 \pm 0.1)\mu_B$ (Ref. 7) and $(0.572 \pm 0.012)\mu_B$ (Ref. 9), but it is likely that these are in error, since in both cases the Rietveld refinement assumed the crystallographic structure to be fluorite at low temperatures, and therefore took no account of the structural distortion. For the secondary (doubled) component of the magnetic structure we obtained $\mu_2 = (0.35 \pm 0.04)\mu_B$ [we disregarded the unreliable $(\frac{5}{2}10)$ reflection when averaging the values of μ_2 obtained from the half-integer reflections]. The uncertainties on our values of μ_1 and μ_2 are dominated by the uncertainty on the magnetic form factor of Pr⁴⁺.

IV. BULK PROPERTIES

We now present measurements of some of the bulk properties of PrO₂: magnetic susceptibility, specific heat capacity, and electrical conductivity. These provide support for the findings of the neutron diffraction experiments described above and reveal clues as to the origin of the structural distortion.

A. Magnetic susceptibility

We measured the magnetic susceptibility of PrO₂ using a commercial superconducting quantum interference device magnetometer, with a powder sample of mass 270 mg. The measurements were made using the reciprocating sample option, with an applied field of $H=1$ T. Data were taken while cooling in steps from $T=350$ K to $T=2$ K, with a delay to allow temperature equilibration at each step. A plot of the molar susceptibility (per mole Pr) is shown in Fig. 11. The inset shows the inverse molar susceptibility. Three features are evident. First, there is a peak at $T=14$ K, due to antifer-

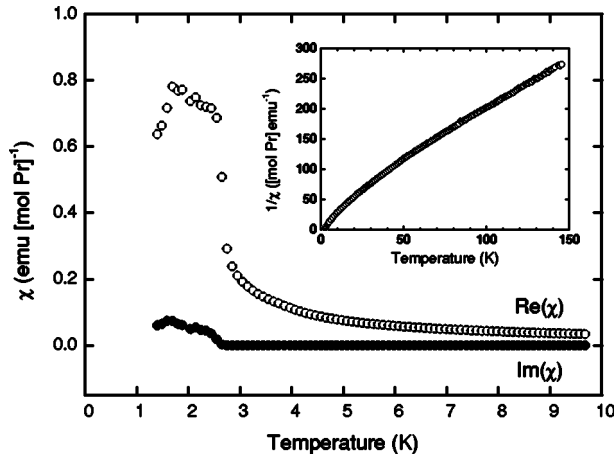


FIG. 12. ac magnetic susceptibility of Pr_6O_{11} powder. The real and imaginary parts of the molar susceptibility are plotted in the main graph, and the inverse of the real part of the molar susceptibility is shown in the inset. The signal in the imaginary part below $T=2.5$ K indicates dissipation accompanying the transition.

romagnetic ordering. Second, there is a change in gradient at $T=122\pm 2$ K which is seen most clearly in the inverse susceptibility. Following our structural investigation we can identify this with the internal distortion at T_D . This anomaly had not been noticed in previous measurements,^{15,16} due to the intrinsic noise present. Third, there is an upturn in the susceptibility below $T\approx 6$ K which is due to the presence of a small amount of Pr_6O_{11} in the sample. We demonstrate this in Fig. 12, which shows a plot of the magnetic susceptibility of Pr_6O_{11} measured by ac susceptometry with a powder sample of mass 327 mg. Between 1.5 K and 2.5 K there is evidence for a magnetic transition with glassy characteristics. At 2 K the molar susceptibility (per mole Pr) of Pr_6O_{11} is ~ 100 times that of PrO_2 , so the upturn below 6 K in the PrO_2 susceptibility is consistent with the 1% Pr_6O_{11} impurity known to be present in the sample. There is no feature in the Pr_6O_{11} susceptibility at T_D .

We used our measurement of the PrO_2 susceptibility to calculate the effective paramagnetic moment of the Pr ion at various temperatures, assuming that the susceptibility obeys the Curie-Weiss law for an antiferromagnet above T_N :

$$\chi^{\text{mol}} = \frac{\mu_{\text{eff}}^2 N_A}{30k_B(T + \theta)}, \quad (7)$$

where χ^{mol} is the molar magnetic susceptibility, θ is the Weiss constant, N_A is Avogadro's number, k_B is Boltzmann's constant, and μ_{eff} is the effective paramagnetic moment of the Pr ion. χ^{mol} is in cgs units [$\text{emu} (\text{mol Pr})^{-1}$], as dictated by convention, whereas the quantities on the right hand side of Eq. (7) are in SI units. The conversion factor from SI to cgs units is incorporated into the right hand side.

Over the temperature range $T=250\text{--}350$ K we obtained $\mu_{\text{eff}}=2.32 \mu_B$. This is close to the value of $2.54 \mu_B$ expected for a free Pr^{4+} ion. Below T_D the gradient of the inverse susceptibility first decreases then increases, causing μ_{eff} to decrease. This indicates a reduction in the number of magnetic degrees of freedom, which is probably caused by a

lifting of the degeneracy of the crystal field ground state by the structural distortion (it is generally accepted that the ground state is a Γ_8 quartet in the fluorite phase).^{7,8}

Although an anomaly at $T=122$ K had not been noticed in previous measurements, the curvature of the susceptibility trace below this temperature had been noticed previously by Kern.¹⁶ When attempting a crystal field analysis he found that his data could not be fitted well with a crystal field of cubic symmetry. He proposed that the oxygen ions surrounding the Pr ion did not in fact form a cube, but that the two at opposite ends of the body diagonal were displaced outward along the (111) direction, causing a splitting of the Γ_8 crystal field level into two doublets. Using this modified structure he obtained a good fit to his data over the whole temperature range 0–300 K. He calculated the splitting of the Γ_8 level to be 28.8 meV.

The significance of this result was later dismissed¹⁵ because the sample used did not exhibit a clear antiferromagnetic transition. Although a discontinuity was observed at 14 K, the susceptibility continued to rise at lower temperatures. The sample had been prepared from a starting material of Pr_6O_{11} by annealing at a temperature of 360 °C under 5 atm of oxygen pressure. These conditions lie close to the border, on a temperature-pressure diagram, of the regions in which the PrO_2 and Pr_6O_{11} phases are stable, so it is likely that the sample was not single-phase PrO_2 . However, x-ray diffraction showed that it had a lattice parameter of 5.393 ± 0.007 Å, which agrees well with the accepted value for PrO_2 of 5.393 ± 0.001 Å, and is much less than the value for Pr_6O_{11} of 5.468 Å.¹⁷ This suggests that the sample was mostly PrO_2 , but contained enough of the Pr_6O_{11} phase to partially obscure the antiferromagnetic transition. By adding proportions of our susceptibility data for Pr_6O_{11} and PrO_2 , and comparing the results with the data obtained by Kern, we estimate that his sample contained $\sim 20\%$ Pr_6O_{11} .

Since we believe that Kern's sample was predominantly PrO_2 , and we have now obtained direct evidence for an internal distortion of the oxygen sublattice below $T_D=120$ K, we believe that his original crystal field analysis, in particular the 28.8 meV splitting of the Γ_8 crystal field ground state, is still of some relevance below T_D .

B. Specific heat capacity

We measured the specific heat capacity of PrO_2 by the relaxation method¹⁸ using a laboratory-built calorimeter. The sample was a disk-shaped pressed pellet of PrO_2 powder of diameter 10 mm, thickness 1 mm, and mass 83 mg, which was mounted on the sapphire sample platform of the calorimeter using a small amount of Apiezon grease (high-thermal-conductivity grease).

The measurements were made over a temperature range of 2.4 K to 23 K. We measured the heat capacity of the sapphire platform first and then the heat capacity of the sample and platform combined. We obtained the heat capacity of the sample alone by subtracting the former from the latter. Finally, we obtained the specific heat capacity of the sample by dividing by the sample mass.

Figure 13 shows a plot of the specific heat capacity of PrO_2 versus temperature. The experimental uncertainty is es-

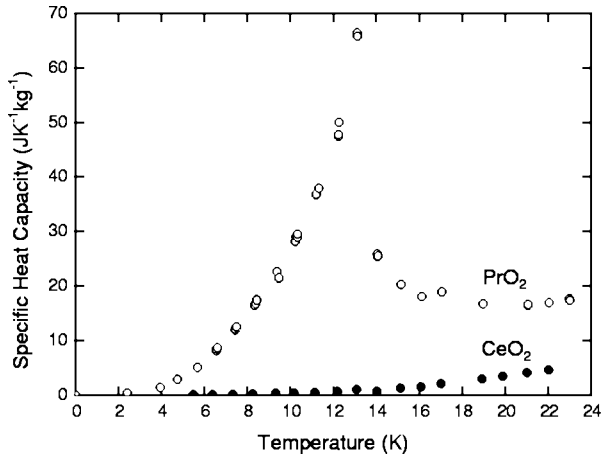


FIG. 13. Specific heat capacity of PrO₂ and CeO₂. The white circles are the PrO₂ data and the black circles are the CeO₂ data. The CeO₂ data provide a good estimate of the phonon contribution to the PrO₂ specific heat.

estimated to be $\sim 5\%$. A lambda anomaly due to the antiferromagnetic ordering is observed at ~ 13.5 K. This is superimposed on the contribution to the specific heat from vibrations of the crystal lattice.

The specific heat capacity of a pressed pellet of CeO₂ powder (commercially obtained) was also measured. This sample had mass 81 mg and was of similar shape to the PrO₂ sample. Since CeO₂ is nonmagnetic, but has the same crystal structure, a similar lattice parameter and similar formula mass to PrO₂, it provides a good estimate of the contribution of the crystal lattice to the PrO₂ specific heat. The CeO₂ data is plotted with the PrO₂ data in Fig. 13.

To determine the degeneracy of the crystal field ground state in PrO₂, we used our measurement of the specific heat capacity to calculate the change in magnetic entropy on passing through the magnetic transition. The specific entropy is related to the specific heat capacity by the formula

$$s(T) = \int_0^T \frac{c}{T} dT, \quad (8)$$

where c is the specific heat and s is the change in specific entropy between $T=0$ and a finite temperature T . The total specific entropy of PrO₂ (magnetic entropy + lattice contribution) was obtained from the specific heat data by dividing by T and then integrating by the extended trapezoidal rule.¹¹ This gave

$$\Delta s_{\text{total}} = \int_0^{23} \frac{c(\text{PrO}_2)}{T} dT = 32.9 \text{ J K}^{-1} \text{ kg}^{-1}. \quad (9)$$

To obtain the change in magnetic entropy it was necessary to subtract off the lattice contribution. This was estimated using the CeO₂ data:

$$\Delta s_{\text{lattice}} = \int_0^{23} \frac{c(\text{CeO}_2)}{T} dT = 1.7 \text{ J K}^{-1} \text{ kg}^{-1}. \quad (10)$$

By subtracting Eq. (10) from Eq. (9) we obtained the change in magnetic entropy:

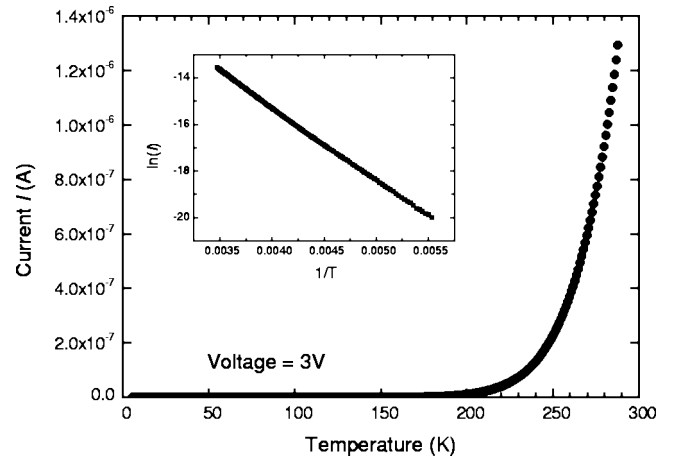


FIG. 14. Current I through a single crystal of PrO₂ at a constant voltage of 3 V. The conductivity is proportional to I . The inset shows $\ln I$ against $1/T$.

$$\Delta s_{\text{magnetic}} = \Delta s_{\text{total}} - \Delta s_{\text{lattice}} = 31.2 \text{ J K}^{-1} \text{ kg}^{-1}. \quad (11)$$

From Boltzmann's law,

$$\Delta s_{\text{magnetic}} = nk_B \ln g, \quad (12)$$

where n is the number of magnetic ions per unit mass (for PrO₂, $n=3.48 \times 10^{24} \text{ kg}^{-1}$) and g is the degeneracy of the ground state above T_N (below T_N the degeneracy is lifted). The entropy changes predicted for a quartet ($g=4$) and a doublet ($g=2$) ground state are $66.7 \text{ J K}^{-1} \text{ kg}^{-1}$ and $33.3 \text{ J K}^{-1} \text{ kg}^{-1}$, respectively. The measured change (11) suggests that the ground state is a doublet. This finding supports a distortion of the crystal structure, which would lift the degeneracy of the Γ_8 quartet below T_D . An extension of the specific heat capacity measurement up to room temperature, to look for an anomaly near 120 K, would be eminently worthwhile.

C. Electrical conductivity

We measured the electrical conductivity of PrO₂ as a function of temperature using a simple probe designed for use with a helium cryostat. Two thin gold wires were attached to opposite sides of the single crystal sample using silver conducting paint (attempts to attach four wires to the tiny crystal were unsuccessful, due to the difficulty in achieving good electrical contact while keeping the contacts separate). The crystal was glued to the copper base of the probe with GE varnish to ensure good thermal contact.

Four-terminal measurements were made of the resistance of the sample + gold wires (this was justified, since the resistance of the crystal was much greater than the resistance of the gold wires) over a temperature range from 5.8 K to 288 K. The temperature was increased in steps, allowing the sample to equilibrate at each new setpoint. Figure 14 shows a plot of current against temperature at a voltage of 3 V. Below $T \sim 180$ K the current became too small to measure reliably. We were unable to determine the absolute value of the electrical conductivity because the shape of the crystal was irregular and its dimensions were not known exactly.

The inset to Fig. 14 shows that the conductivity has an activated behavior, at least over the temperature range 180–288 K. To determine the activation energy we fitted our data using the Arrhenius form:

$$I = I_0 \exp\left(-\frac{E_a}{k_B T}\right), \quad (13)$$

where I is the current and E_a is the activation energy. We extracted E_a from several runs, each measured at a different constant voltage (between -5 V and $+5$ V), and took the mean of these values to obtain $E_a = 0.262 \pm 0.003$ eV for the temperature range 180–288 K. This is much smaller than the band gap of ~ 2.5 eV predicted by band structure calculations,¹⁹ and is also smaller than the activation energies of other PrO_x materials, which have been reported in the range 0.4–1 eV.^{20–22}

Possible mechanisms for electrical conductivity in PrO_2 are (i) ionic conductivity, (ii) intrinsic electronic conductivity due to hopping between Pr sites, and (iii) extrinsic electronic conductivity due to impurities. Compounds with the fluorite structure often exhibit ionic conduction when vacancies caused by Schottky or Frenkel defects allow the oxygen ions to hop from site to site. However, at room temperature the number of thermally induced defects is very small, so ionic conductivity in PrO_2 is unlikely to be important in this temperature range. It has been suggested that ionic conductivity in PrO_x materials is significant only above ~ 900 K.^{21,22} Therefore, it is most likely that the conductivity in PrO_2 is electronic. Given the small activation energy found here, the mechanism warrants further investigation.

V. DISCUSSION AND CONCLUSIONS

We have presented neutron diffraction experiments on single-crystal PrO_2 , which reveal an internal distortion of the oxygen sublattice at $T_D = 120 \pm 2$ K and a related component of the magnetic structure below $T_N = 13.5 \pm 0.2$ K. The displacements of the oxygen ions are five times as large as those observed in UO_2 ,¹² and this is reflected in the high value of the transition temperature. The observation that both the distorted crystallographic structure and the related component of the magnetic structure have a unit cell that is doubled along one crystal axis with respect to the fluorite structure suggests that the displacement of the oxygen ions affects the magnetic ordering of the Pr sublattice.

Our measurement of the specific heat capacity indicates that the crystal field ground state of the Pr $4f$ electron is a

doublet, consistent with the lowering of the local symmetry of the Pr site. This raises the question of what mechanism drives the structural distortion. The most obvious answer is that the electronic energy is reduced by a collective Jahn-Teller distortion at the expense of a small penalty in elastic energy. Another possibility is that the distortion is a consequence of a quadrupolar ordering of the Pr $4f$ orbitals. Intuitively this would seem an unlikely mechanism, since the coupling between electric quadrupoles would be expected to be too weak to cause an orbital ordering at a temperature as high as 120 K. Nevertheless, there is evidence for a degree of Pr $4f$ –O $2p$ hybridization in PrO_2 ,^{23,24} and such a covalency effect could provide a mechanism for aligning the $4f$ orbitals.

The splitting of the ground state could also partly explain the observation of an ordered magnetic moment smaller than that associated with the Γ_8 quartet ground state of cubic symmetry. On the other hand, we have previously reported a broad continuum of magnetic scattering in the excitation spectrum of PrO_2 , which we believe arises from a strong magnetoelastic coupling.⁸ This coupling would tend to quench magnetic degrees of freedom and reduce the size of the ordered moment by the dynamic Jahn-Teller mechanism. From the experimental evidence available so far it seems likely that both the static and dynamic Jahn-Teller effects are important in PrO_2 , but it is not clear which of the two is dominant at low temperatures.

In work that we will report elsewhere,²⁵ we have found that the application of a magnetic field in the distorted phase at $T < T_D$ produces striking hysteresis effects in both the magnetic structure and the magnetization. The totality of results that have emerged in recent years suggests that a strong interplay between electronic and lattice degrees of freedom exists in PrO_2 and influences its properties, perhaps in unexpected ways.

ACKNOWLEDGMENTS

We would like to thank P. Santini for insightful discussions, and D. Prabhakaran and F. Wondre for help with sample preparation and characterization. We would also like to thank J. Jensen for suggesting the chiral model for the distorted crystal structure and making many other helpful comments. We are also grateful to M. Enderle and K. Kiefer for advice on the design of the calorimeter. Financial support by the EPSRC is acknowledged.

*Electronic address: carol.webster@npl.co.uk

¹Y. Tokura and N. Nagaosa, *Science* **288**, 462 (2000).

²E. Saitoh, S. Okamoto, K. T. Takahashi, K. Tobe, K. Yamamoto, T. Kimura, S. Ishihara, S. Maekawa, and Y. Tokura, *Nature (London)* **410**, 180 (2001).

³G. Khaliullin and S. Maekawa, *Phys. Rev. Lett.* **85**, 3950 (2000).

⁴G. Khaliullin, *Phys. Rev. B* **64**, 212405 (2001).

⁵P. Santini, R. Lémanski, and P. Erdős, *Adv. Phys.* **48**, 537 (1999).

⁶J. A. Paixão, C. Detlefs, M. J. Longfields, R. Caciuffo, P. Santini, N. Bernhoeft, J. Rebizant, and G. H. Lander, *Phys. Rev. Lett.* **89**, 187202 (2002).

⁷S. Kern, C.-K. Loong, J. Faber, Jr., and G. H. Lander, *Solid State Commun.* **49**, 295 (1984).

⁸A. T. Boothroyd, C. H. Gardiner, S. J. S. Lister, P. Santini, B. D. Rainford, L. D. Noailles, D. B. Currie, R. S. Eccleston, and R. I. Bewley, *Phys. Rev. Lett.* **86**, 2082 (2001).

- ⁹C. H. Gardiner, A. T. Boothroyd, S. J. S. Lister, M. J. McKelvy, S. Hull, and B. H. Larsen, *Appl. Phys. A: Mater. Sci. Process.* **74**, S1773 (2002).
- ¹⁰M. McKelvy and L. Eyring, *J. Cryst. Growth* **62**, 635 (1983).
- ¹¹W. H. Press, S. A. Teukolsky, W. T. Vetterling, and B. P. Flannery, *Numerical Recipes in C: The Art of Scientific Computing*, 2nd ed. (Cambridge University Press, Cambridge, U.K., 1992).
- ¹²J. Faber, Jr., and G. H. Lander, *Phys. Rev. B* **14**, 1151 (1976).
- ¹³P. Burlet, J. Rossat-Mignod, S. Quezel, O. Vogt, J. C. Spirlet, and J. Rebizant, *J. Less-Common Met.* **121**, 121 (1986).
- ¹⁴J. Jensen (unpublished).
- ¹⁵J. B. MacChesney, H. J. Williams, R. C. Sherwood, and J. F. Potter, *J. Chem. Phys.* **41**, 3177 (1964).
- ¹⁶S. Kern, *J. Chem. Phys.* **40**, 208 (1964).
- ¹⁷L. Eyring and N. C. Baenziger, *J. Appl. Phys.* **33**, 428 (1963).
- ¹⁸R. Bachmann *et al.*, *Rev. Sci. Instrum.* **43**, 205 (1972).
- ¹⁹D. D. Koelling, A. M. Boring, and J. H. Wood, *Solid State Commun.* **47**, 227 (1983).
- ²⁰L. Eyring, *Handbook on the Physics and Chemistry of Rare Earths* (North-Holland, Amsterdam, 1979), pp. 337–399.
- ²¹T. Arakawa, A. Kabumoto, and J. Shiokawa, *J. Less-Common Met.* **115**, 281 (1986).
- ²²G. V. Subba Rao, S. Ramdas, P. N. Mehrotra, and C. N. R. Rao, *J. Solid State Chem.* **2**, 377 (1970).
- ²³R. C. Karnatak, J.-M. Esteve, H. Dexpert, M. Gasgnier, P. E. Caro, and L. Albert, *Phys. Rev. B* **36**, 1745 (1987).
- ²⁴A. Bianconi, A. Kotani, K. Okada, R. Giorgi, A. Gargano, A. Marcelli, and T. Miyahara, *Phys. Rev. B* **38**, 3433 (1988).
- ²⁵C. H. Gardiner, A. T. Boothroyd, M. J. McKelvy, G. J. McIntyre, and K. Prokeš, following paper, *Phys. Rev. B* **70**, 024416 (2004).
- ²⁶Averaging over symmetry-equivalent domains in Eq. (2) means that we compare the observed intensity $I(hkl)_{\text{obs}}$ with the calculated intensity $1/6[I(hkl)_{\text{calc}} + I(klh)_{\text{calc}} + I(lhk)_{\text{calc}} + I(\bar{h}lk)_{\text{calc}} + I(\bar{k}hl)_{\text{calc}} + I(\bar{l}kh)_{\text{calc}}]$, where h , k , and l are in the cubic cell. This accounts for threefold twinning around the cubic $\langle 111 \rangle$ direction and reflection across the cubic (011) plane.